Shaping the nonlinear emission pattern of a dielectric nanoantenna by integrated holographic gratings

Lavinia Ghirardini,[1] Giuseppe Marino,[2] Valerio F. Gili,[2] Ivan Favero,[2] Davide Rocco,[3] Luca Carletti,[3] Andrea Locatelli,[3] Costantino De Angelis,[3,4] Marco Finazzi,[1] Michele Celebrano,[1] Dragomir N. Neshev,[5] and Giuseppe Leo[2,*]

[1]*Department of Physics, Politecnico di Milano, Piazza Leonardo Da Vinci 32, 20133 Milano, Italy*

[2]*Laboratoire Matériaux et Phénomènes Quantiques, Université Paris Diderot, CNRS UMR 7162, 10 rue A. Domon et L. Duquet, 75013 Paris, France*

[3]*Department of Information Engineering, University of Brescia, Via Branze 38, Brescia 25123, Italy*

[4]*National Institute of Optics (INO), Via Branze 45, Brescia 25123, Italy*

[5]*Nonlinear Physics Centre, Research School of Physics and Engineering, The Australian National University, Canberra ACT 2601, Australia*

**Corresponding author: giuseppe.leo@univ-paris-diderot.fr*

KEYWORDS Second Harmonic Generation, Beaming, Collection Efficiency, Nonlinear nanoantennas, Gratings.

ABSTRACT

We demonstrate the shaping of the second-harmonic (SH) radiation pattern from a single AlGaAs nanodisk antenna using coplanar holographic gratings. The SH radiation emitted from the antenna towards the - otherwise forbidden - normal direction can be effectively redirected by suitably shifting the phase of the grating pattern in the azimuthal direction. The use of such gratings allows increasing the SH power collection efficiency by two orders of magnitude with respect to an isolated antenna and demonstrates the possibility of intensity-tailoring for an arbitrary collection angle. Such reconstruction of the nonlinear emission from nanoscale antennas represents the first step towards the application of all-dielectric nanostructures for nonlinear holography.

MAIN TEXT

Nanoantennas funnel propagating optical radiation into subwavelength field modes localized at the nanoscale and are very efficient transducers for both emission and detection of light [1-4], sensing [5], optical tomography [6] and quantum sources [7]. Efficient conversion of optical radiation is made possible by engineering them with an accuracy of few nanometers, which is enabled by current nanoscale fabrication techniques, such as electron-beam lithography or self-assembly, based respectively on top-down and bottom-up approaches. Due to the intense field enhancement associated with the high localization of surface plasmons, metallic nanoantennas have long been considered as the most efficient linear [8] and nonlinear transducers [9-11]. However, all-dielectric optical antennas have recently demonstrated higher effective control of the far-field scattering [12], thanks to (i) extremely low losses and (ii) the ability to sustain both electric and magnetic multipolar resonant optical modes. These two characteristics have endowed researchers with a large flexibility to further engineer the nonlinear radiation pattern of dielectric nanostructures [13,14]. Recently, efficient SH emission of the order of 10^{-5} [15] and 10^{-4} [16] was reported in AlGaAs nano-cylinders, thanks to the high second-order susceptibility of this material. Despite these record-higher efficiencies, the complex SH radiation pattern presents a major limitation, due to the symmetry of the AlGaAs nonlinear susceptibility tensor: a null in the forward and backward directions for normal-incidence fundamental-wave (FW) illumination [17]. The phase control of SH scattered light in these nanoantennas remains unexplored to date, although it is a promising way to provide on-chip SH normal emission with a simple normally incident excitation, and to further tailor such emission for arbitrary collection angles. Importantly, the shaping of the nonlinear wavefront excited with a simple pumping configuration has useful applications, e.g. in single photon

sources [18], nonlinear imaging [19] and holography, where low-power, low-cost components and directional high-resolution are required.

In this work, we demonstrate phase control of the nonlinear emission of all-dielectric nanostructures, leading to intensity-tailoring of the SH emission for arbitrary collection angles. This is achieved by carving dielectric holographic gratings via electron-beam lithography in the proximity of the nanoantennas. The axial-symmetry of the grating structure enables the redirection of the coherent SH radiation emitted at grazing angles from the optical antenna towards its normal. In addition, by both varying the grating symmetry and the pump polarization, the redirection of the lateral SH emission can be effectively tailored in the perspective of encoding SH holographic patterns into the far field.

Although the confinement of the FW emitted light to very narrow angles and the enhancement of collection efficiency have already been the subject of intense study in the field of single photon emitters [20-22], to the best of our knowledge, this is the first demonstration of a method for wavefront manipulation of the near-field SH generation (SHG) from a high-symmetry sub-wavelength nanoantenna. Our reconstruction of the nonlinear emission is a rugged alternative to the tilting of FW pump beam [23,24], where oblique incidence enables an increase of the dipolar contribution in the SH scattering, leading to a radiation pattern that has a maximum along the backward and forward normal directions.

A schematic of our nonlinear transducer is reported in Figure 1a. The $Al_xGa_{1-x}As$ dielectric antenna is a nanocylinder of radius r = 220 nm and height h = 400 nm, surrounded by three concentric $Al_xGa_{1-x}As$ ridges at a distance d, and with height t_g. Two different semicircular gratings are fabricated, spatially shifted by a distance s, which diffract the SH radiation emitted by the cylinder in opposite directions. We set $t_g = h$ and d = 500 nm to ensure that the grating

structure does not affect the linear scattering behavior of the cylinder at the FW frequency. Additionally, we choose an Al molar fraction x = 0.18 to ensure transparency at both the pump and SH wavelengths, here λ_{FW} = 1.57 μm and λ_{SH} = 0.78 μm, respectively. The concentric grating has been optimized to redirect vertically the in-plane antenna radiation (Fig. 1c), which otherwise shows an odd axial symmetry and a maximum emission intensity at a large off-axis angle, Fig. 1b. Design guidelines are based on evaluating the radiation in the *xz*-plane, ignoring the azimuthal dependence of the SHG light, as depicted in Fig. 1a. For far-field observations and using a polar coordinate system centered on the nanodisk, with r the radial distance and θ the polar angle, we can express the total emitted far-field at the SH wavelength as:

$$E_T^{SH}(r,\theta) = E_g^{(1)}(r,\theta) + E_g^{(2)}(r,\theta) + E_d^{SH}(r,\theta), \quad (1)$$

where $E_g^{(j)}$ is the field radiated by the diffraction grating j=1,2, and E_d^{SH} is the SH emission from the nanodisk. We can simplify Eq. (1) by assuming that the two gratings are identical and host negligible nonlinear currents. In this case, the field incident on each grating is given by the nanodisk in-plane emission at the SH wavelength. Therefore the SH radiation diffracted by the gratings in the normal direction (i.e. θ = 0) parallel to the z axis is given by the following expression: $E_g^{(1)}(z,0) = a_1 G(0) e^{-ik_0 z}$, $E_g^{(2)}(z,0) = a_2 G(0) e^{-ik_0 z}$, where $G(0)$ is the grating response function at θ = 0 that depends solely on the geometrical parameters of the grating and k_0 is the free-space wavenumber. The incident fields on the grating are given by $a_1 = E_d^{SH}(\pi/2) e^{-ik_x d}$ and $a_2 = E_d^{SH}(-\pi/2) e^{-ik_x (d+s)}$, k_x being the in-plane propagation wavevector. Since the SH radiation from the disk in the *xz*-plane exhibits an odd symmetry, we have that $E_d^{SH}(-\pi/2) = -E_d^{SH}(\pi/2)$. Therefore, the electric field radiated in the normal

direction by grating 2, can be expressed as $E_g^{(2)}(z,0) = G(0)\, E_d^{SH}\left(-\frac{\pi}{2}\right) e^{-ik_x d} e^{-i\beta} = -E_g^{(1)}(z,0) e^{-i\beta}$, where $\beta = k_x s$ is the phase difference between the SH fields incident on the two gratings. Substituting these relations in Eq. (1), we can now obtain a new expression for the total field radiated along the z axis by the structure: $E_T^{SH}(z,0) = \left[G(0) E_d^{SH}\left(\frac{\pi}{2}\right)\left(1 - e^{-i\beta}\right) + E_d^{SH}(0)\right] e^{-ik_0 z}$. Our first aim is to maximize the SH radiation in the backward direction (*i.e.*, $\theta = 0$). Due to symmetry, the SH emission from the nanodisk is strictly forbidden in the normal (forward or backward) direction [22,23], hence $E_d^{SH}(0) = 0$. Thus, the radiated intensity by the proposed structure is proportional to:

$$|E_T^{SH}(z,0)|^2 = 2\left|G(0) E_d^{SH}\left(\frac{\pi}{2}\right)\right|^2 [1 - \cos(\beta)]\,, \qquad (2)$$

showing that the total intensity in the normal direction depends only on the interference pattern generated by the gratings, which is governed by the phase difference β. From Eq. (2), it follows that the condition of optimal length s for a normal SH emission in air is:

$$s_{max} = (2m+1)\frac{\lambda}{2}, \text{ with } m = 0, \pm 1, \pm 2, \ldots\,. \qquad (3)$$

SHG in the normal direction can thus be obtained only with a non-centrosymmetric grating, which provides the necessary symmetry reduction. In fact, we can observe that if s = 0 nm, then β = 0 and, from Eq. (2) we obtain $|E_T^{SH}(0)|^2 = 0$ (see schematic in Fig. 1b). In practice, two spatially-displaced (by a distance s) halves of the grating introduce a phase shift between the respective in-plane SH emitted light, enabling constructive interference along the normal direction [25]. This allows one to efficiently reshape the quadrupolar SH-emitting mode, and thus to couple the far-field radiation pattern onto the propagation direction normal to the surface,

as illustrated in Fig. 1c. Further engineering of the radiation pattern can be obtained by redirecting the in-plane waves from different azimuthal directions to interfere in the far-field with a complex designer phase, following the principles of leaky-wave holographic antennas, known in radio-physics [26]. Thus, one can achieve the formation of complex holographic images from a single nonlinear SH antenna, only limited by the conditions of Eq. (1).

Aided by numerical simulations, we have designed a grating period of 340 nm, with 85% duty cycle, corresponding to a width of each ridge of the grating equal to 260 nm. Based on these parameters, we can estimate that the optimal shift between the two half-gratings to maximize the SH emission in the backward direction is s = 290 nm. This value is slightly different from the estimations obtained from Eq. (3) since it is obtained from full-vectorial simulations exploiting the finite element method in the frequency domain implemented in the COMSOL software [15] and taking into account the phase velocity of the in-plane propagating waves. Nevertheless, although simplified, our analytical design procedure provides an excellent starting point for the optimization of the structure.

Our samples are grown by molecular-beam epitaxy on a [100] non-intentionally doped GaAs wafer, with a 400 nm layer of $Al_{0.18}Ga_{0.82}As$ on top of a 1 μm thick $Al_{0.98}Ga_{0.02}As$ substrate (the latter being sandwiched between two thin matching layers with grading Al composition). MaN-2401 e-beam negative-tone resist is then spin-coated on the surface of the sample, followed by electron-beam lithography to define the nanostructures. To correct proximity effects stemming from the high-density grating features, we vary the e-beam dose between 90 and 120 $\mu C/cm^2$. After development, the patterns are transferred on the $Al_{0.18}Ga_{0.82}As$ layer with $SiCl_4$:Ar-assisted dry inductively-coupled plasma-reactive-ion etching (ICP-RIE). The

etching process reveals the Al-rich substrate, which is then selectively oxidized at 390 °C for 30 minutes.

The experimental characterization of our nonlinear beam collimator has been carried out with a confocal nonlinear setup. Femtosecond pulses ($\Delta t \sim 100$ fs) from a near-infrared fiber laser, at a central wavelength of 1560 nm are sent through a half-wave plate to obtain the desired polarization for the experimental measurement. The beam is then focused on the sample through a 0.7 NA long-working-distance microscope objective. The nonlinear emission from the sample is collected in reflection geometry, through the same objective and sent to the detection path by a dichroic mirror that filters out the backward SH from the fundamental wavelength. Before being imaged on a cooled CCD camera, the signal from the sample is further filtered using a combination of short-pass (cut-off ~ 800 nm) and a long-pass (cut-on ~ 600 nm) filters to remove any third-harmonic emission from the nanoantenna and any possible signal contribution from the substrate. The real-space SH emission from the sample is then imaged directly on the camera, while an additional lens images the emission pattern in the Fourier space in the objective back focal plane. A linear polarizer can be inserted in the detection path to select the emission contribution co- or cross-polarized with respect to the pump. The input FW is linearly polarized along the *y*-axis (Fig. 1).

We first consider an isolated AlGaAs nanocylinder, as a reference structure. We numerically model its optical response using the finite element method in the frequency domain. In our simulations, the disk is assumed to be placed on a substrate with refractive index $n_s = 1.6$ to mimic the of AlO_x layer in our wavelength range of operation. For the dispersion of the refractive index of $Al_{0.18}Ga_{0.82}As$, we used the analytical model proposed in [27], which was

derived by comparison with measurements. To emulate the experimental conditions more accurately, we excite the nanodisk by a focused monochromatic Gaussian beam with a FWHM of 2 μm. The second-order nonlinear optical response associated with the SHG is modeled using the nonlinear polarization induced by the quadratic $\chi^{(2)}$ nonlinearity. Since AlGaAs has a zinc-blende crystalline structure, the only non-vanishing terms of the nonlinear susceptibility tensor $\chi_{ijk}^{(2)}$ are for $i \neq j \neq k$, which are all assumed to have a value of 100 pm/V [28].

Figure 2a shows the calculated scattering cross-section for an isolated nanocylinder, as a function of the FW wavelength. A multipolar decomposition, performed using the polarization currents induced inside the disk, suggests that the resonance around 1.6 μm is mainly due to a magnetic dipole (MD) and an electric dipole (ED) contribution. The MD character of the resonance can also be seen from the electric field map in Fig. 2b, which shows the electric field loop, partially extending into the AlOx substrate. The quadrupolar scattering components provide only a minor contribution to the overall SH emission, which tends to grow slightly when the wavelength is reduced. For the sake of clarity, here we limit our analysis to the frequency range dominated by the magnetic resonance. The odd axial symmetry of the MD mode is directly transferred to the emission pattern of the AlGaAs cylinder, which shows a maximum emission intensity at a large off-axis angle (Fig. 2c), consistent with previous works [16,29]. As mentioned above, the null radiation in the forward direction comes directly from the symmetry of the nonlinear tensor and from the illumination axis being perpendicular to the substrate. The experimentally measured radiation pattern is in excellent agreement with simulations, showing a typical far-field doughnut-shape beam, which is mainly cross-polarized with respect to the pump beam, as previously reported [16,29,30].

Next, we tested the radiation pattern of an AlGaAs pillar with the same geometrical parameters as the reference but coupled to an in-plane holographic grating. As shown in Fig. 3a, the radiation of the pillar is strongly reshaped by the grating pattern (see the SEM image of the fabricated structure in Fig. 3b) and redirected towards the normal *k*-vectors. Due to the grating scattering of the in-plane SH emission towards the normal direction, the detected radiation pattern becomes mainly co-polarized with the pump beam. While our numerical calculations correctly predict a negligible cross-polarized SH emission, we observe minor differences between theory and experiment which are attributed to both fabrication inaccuracies and the actual nanocylinder height that is about 10% higher than the nominal value, due to the presence of the epitaxial matching layer. It is worth noting that in our experiments the nanoantenna and a small part of the grating are simultaneously excited by the pump beam, which has a focal spot of roughly 2 μm in diameter. In sections I and II of the Supplementary Information (SI) we report numerical calculations identifying the different contributions to the SH radiation pattern of the disk and the grating. The results summarized in Table S1 demonstrate that 76% of the SH radiated within a small numerical aperture (NA = 0.2) above the cylinder is from the redirection of the SH cylinder signal, with only 16% contribution coming from the SH emitted by the grating, and finally 7.5% from the interference between the SH emission of the gratings and the SH of the cylinder. We can thus safely assume that the nonlinear SH emission is mainly due to the nanocylinder, which is resonant to the FW beam, and that the redirection of the SH signal and its co-polarized nature only marginally depend on the nonlinear currents excited in the grating.

The effect of the grating on the pillar radiation pattern can be seen more clearly by evaluating the electric field above the cylinder. Fig. 3c shows simulated and experimental cuts

of the nonlinear emission in the *xz*-plane for both the isolated nanoantenna and the nanoantenna surrounded by the concentric grating. The zero in the emission at the normal direction ($\theta = 0°$) disappears in the presence of the optimized grating. The measured far-field intensity pattern emitted from the structure with the $N = 3$ grating is consistent with our simulations, clearly indicating the collimation of the generated SH field into a narrow, forward-propagating lobe. A comparison of the two SH emissions within a 0.2 NA solid angle leads to a collection power enhancement of about two orders of magnitude for the nanoantenna-grating structure with respect to the isolated nanoantenna. A further figure of merit, accounting for the on-chip footprint cost coming from the grating, is the ratio between the SH power in the normal direction (NA = 0.1) over the surface occupied with and without the gratings, for the geometries as in Figs. 2 and 3. In the case of a nanocylinder surrounded by the optimized three concentric grooves, this figure of merit is a factor 4 higher than that of an isolated pillar.

Figure 4 shows the effect of the incident beam polarization on the beam collimation performed by the grating. A strong collection enhancement of the SH signal in the objective NA is obtained for polarization of the incident light that generates maximum in-plane SHG lobes along the grating symmetry plane (Fig. 4a), while other input polarizations give rise to different emission patterns with lower emission (Fig. 4b and c).

An interesting feature that emerges from our studies, shown in Figure 5, is that, by changing the parameters *d* and *s* of the grating structure, one can engineer the phase shift of the radiation diffracted by the two halves of our grating structure and thus modulate the beam-collimation effect produced by their interference. To better highlight this intensity-tailoring

capability, we report in Fig. B of the SI the percentage of SH intensity emitted from different gratings between the normal direction and the maximum collection angle defined by the NA of the objective. For example, the percentage of intensity emitted within a NA of 0.5 from the non-centrosymmetrical holographic gratings in Fig 3a (Fig. 5a,b) is 80% (70%, 60%) of the total collected intensity. In contrast to this, the original isolated high-symmetry nanoantenna emits 40% of the total collected intensity within the same NA. In addition, in a 0.3 collection NA for example, while the individual pillar directs only 10% of the SHG, in the optimized structure still 50% of the emission can be collected. These results suggest the possibility of designing the diffracting structure surrounding the nonlinear nano-emitter to obtain a nonlinear hologram that would intrinsically differ from the one of Ref. 7. In fact, this can also be seen as a nonlinear holography method, where the image is formed at a different frequency than that of the pump. For example, different patterns resembling a flower or a bird emerge in the far field of our structures for different choices of the design parameters (see Figs. 5a and c, for structures with d = 450 nm and d = 700 nm, respectively) and of the pump polarization (see Fig. 4). Such patterns observed in the far-field of SH emission highlight the potentials for complex engineering of the nonlinear emission from a single nanoantenna.

In summary, we have demonstrated that carving dielectric holographic gratings in the proximity of dielectric nanoantennas enables phase control of the nonlinear wavefront generated by the nanoantennas and tailor SH emission for arbitrary collection angles. More precisely, in-plane dielectric gratings convert the quadrupolar SHG mode from cylindrical dielectric nanoantennas into a dipolar-like emission profile. In this way, we obtain a two-orders-of-magnitude enhancement of the power collection efficiency with respect to an isolated structure, while maintaining a simple normal incident excitation configuration. By

both optimizing the parameters *d* and *s* of the gratings that surround the AlGaAs nanocylinders and tuning the pump polarization, we achieve an effective redirection of the lateral SH emission from AlGaAs nanostructures along the cylinder axis. Our results open new routes to frequency-conversion infrared imaging devices, nonlinear holograms at the nanoscale and miniaturized quantum sources of light.

ACKNOWLEDGMENT

Giuseppe Leo acknowledges Aristide Lemaître (CNRS C2N) for the epitaxial wafers, SATT IdF-Innov, ANR "Science and Engineering of Advanced Materials" (SEAM) Labex and MULTIPLY EU Co-fund program for financial support. The work was partially supported by the Australian Research Council and by the Framework of the Erasmus Mundus NANOPHI Project.

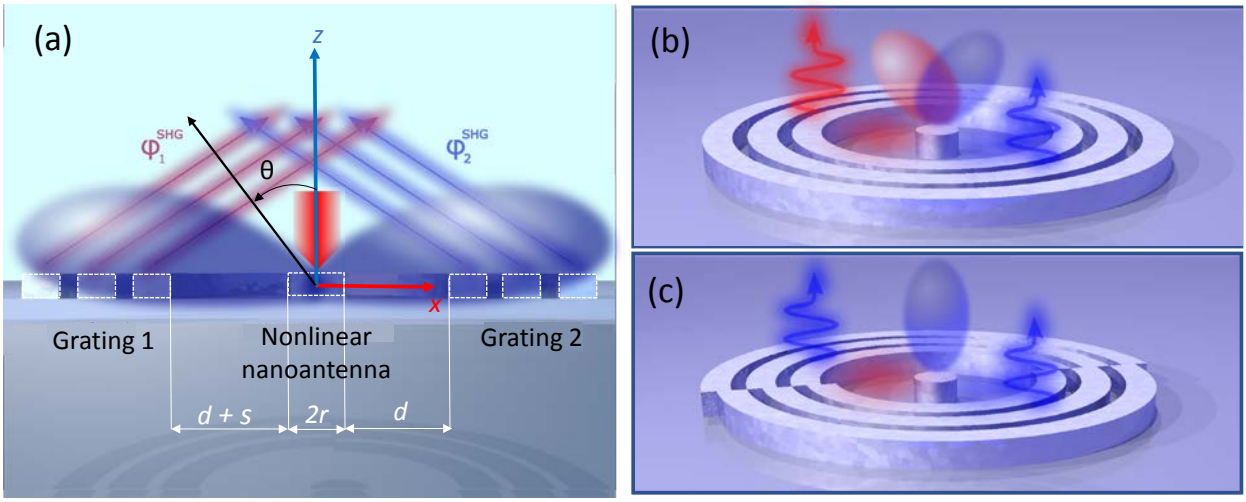

Figure 1. Sample sketch (a) of nonlinear beam collimating structure with parameters d = 500 nm and s = 290 nm. Schematic of the working principle of the SHG redirection process by a holographic grating. The antenna SH radiation that shows a quadrupolar symmetry (b). Light scattered by the two halves of an asymmetric grating remains in opposition of phase, and the corresponding radiation pattern maintains a quadrupolar symmetry. Efficient SH coupling onto the direction normal to the surface is achieved by introducing a phase shift in the light scattered with an asymmetric grating (c), changing the radiation pattern to a dipole one and thus increasing the collection efficiency of the system.

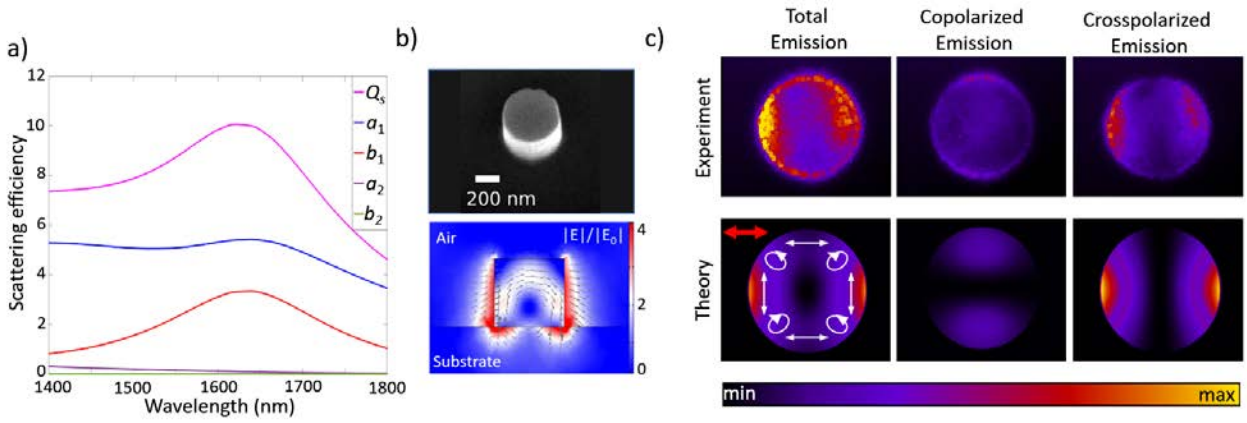

Figure 2. (a) Scattering efficiency (Q_s) spectra for a disk with radius r = 220 nm and height h = 400 nm, with the multipole expansion terms of the optical response. The coefficients a_1, b_1, a_2, and b_2 are due to electric dipole, magnetic dipole, electric quadrupole, and magnetic quadrupole contributions, respectively. The inset shows the electric field distribution inside the disk at the fundamental wavelength λ = 1570 nm. (b) SEM image of the fabricated sample (top) and simulated electric field amplitude (bottom). (c) Experimental (top) and theoretical (bottom) SH emission pattern for the isolated pillar assuming a collection NA= 0.7, decomposed in its contributions co-polarized and cross-polarized with respect to the pump beam. White arrows show the polarization of the emitted radiation while the red arrow represents the input pump polarization

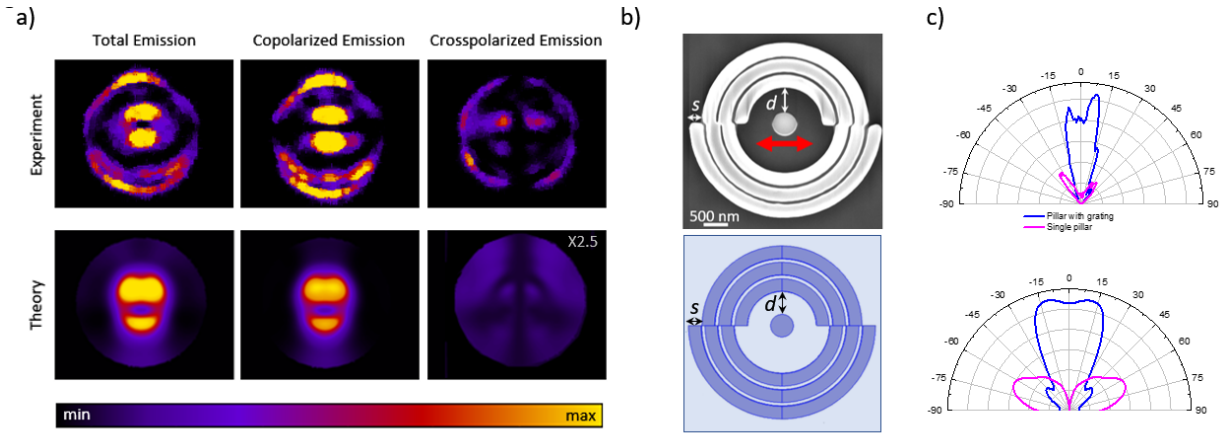

Figure 3. (a) Experimental (top) and theoretical (bottom) SH emission pattern (λ = 785 nm) for the pillar surrounded by our grating structure, assuming a collection NA = 0.7, decomposed in its contributions co-polarized and cross-polarized with respect to the pump beam. (b) SEM image of the fabricated (top) and optimized theoretical structure (bottom). The red arrow indicates the input polarization of the pump beam. (c) Comparison of the experimental (top) and simulated (bottom) SH radiation pattern emitted in the air region for λ = 1570 nm pump wavelength in the case of a single cylinder (purple line) and of cylinder coupled to a N = 3 grooves grating structure (blue line).

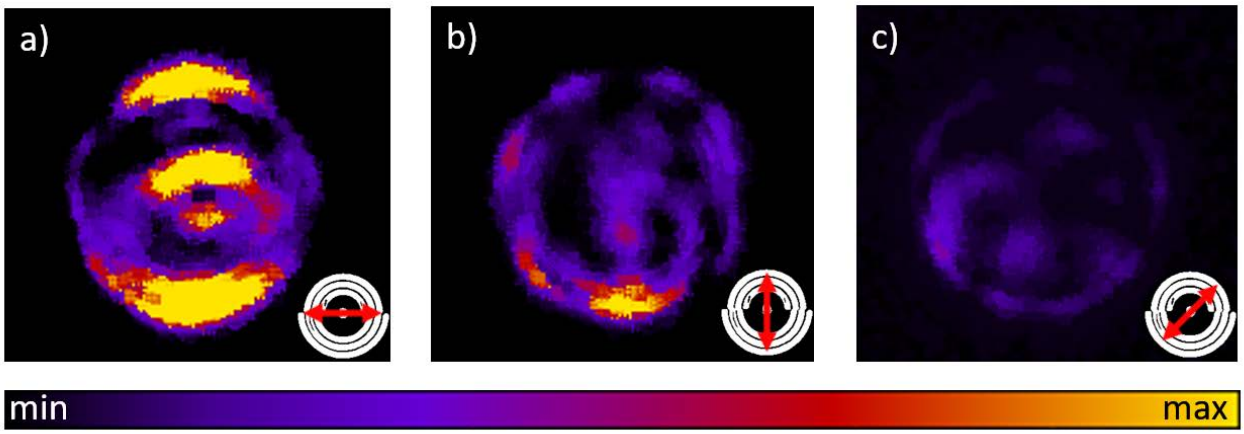

Figure 4. (a) Experimental SH radiation pattern from our grating structure at λ = 785 nm for three different incident pump polarizations: (a) horizontal, (b) vertical and (c) 45°, as shown by the red arrows in the corresponding insets.

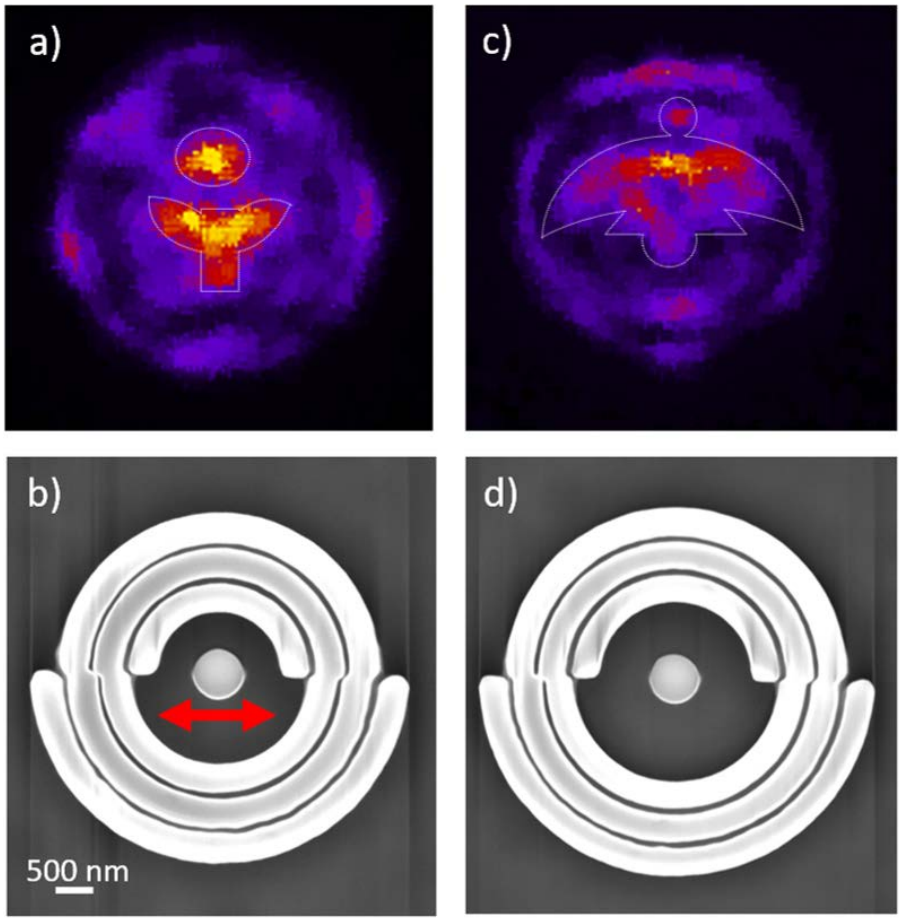

Figure 5. SHG far-fields resembling a flower (a) and a bird (c), obtained with the nanostructures (b), with d = 450 nm, and (d) d = 700 nm, respectively. The red arrow in (b) indicates the incident polarization of the pump beam.

REFERENCES

[1] Novotny, L. *Nature* **2008**, 455, 887.

[2] Koenderink, A. F. *Nano Letters* **2009**, 9, 4228-4233.

[3] Novotny, L.; van Hulst, N. *Nature Photonics* **2010**, 5, 83-90.

[4] Dorfmuller, J.; Dregely, D.; Esslinger, M.; Khunsin, W.; Vogelgesang, R.; Kern, K.; Giessen, H. *Nano Letters* **2011**, 11, 2819-2824.

[5] Wang, P.; Krasavin, A. V.; Nasir, M. E.; Dickson, W.; Zayats, A. V. *Nature Nanotechnol.* **2018**, 13, 159.

[6] Segovia, P.; Marino, G.; Krasavin, A. V.; Olivier, N.; Wurtz, G. A.; Belov, P. A.; Ginzburg P.; Zayats A. V. *Optics Express* **2015**, 23, 30730-8.

[7] Almeida, E.; Bitton, O.; Prior, Y. *Nature Commun.* **2016**, 7, 12533.

[8] Ghenuche, P.; Cherukulappurath, S.; Taminiau, T. H.; van Hulst; N. F., Quidant, R. *Phys. Rev. Lett.* **2008,** 101, 116805.

[9] Berthelot, J., Bachelier, G., Song, M., Rai, P., Des Francs, G. C., Dereux, A., & Bouhelier, A., *Optics Express* **2012**, 20, 10498-10508.

[10] Celebrano, M.; Wu, X.; Baselli, M.; Großmann, S.; Biagioni, P.; Locatelli, A.; De Angelis, C.; Cerullo, G.; Osellame, R.; Hecht, B.; Duò, L.; Ciccacci, F.; Finazzi, M., *Nat. Nanotechnol.* **2015**, 10, 412–417.

[11] Dapap, J. I.; Shan, J.; Eisenthal, K. B.; Heinz, T. F. *Phys. Rev. Lett.* **1999**, 83, 4045-4048.

[12] Kuznetsov, A. I.; Miroshnichenko, A. E.; Brongersma, M. L.; Kivshar, Y. S;, Luk'yanchuk B. *Science* **2016**, 354, 24721-24728.

[13] Shcherbakov, M. R.; Neshev, D. N.; Hopkins, B.; Shoroklhov, A. S.; Staude, I.; Melik-Gaykazyan, E. V.; Decker, M.; Ezhov, A. A.; Miroshnichenko, A. E.; Brener, I.; Fedyanin, A. A.; Kivshar, Y. S. *Nano Letters* **2014**, 14, 6488-6492.

[14] Shorokhov, A. S.; Melik-Gaykazyan E. V.; Smirnova, D. A.; Hopkins, B.; Chong, K. E.; Choi, D. K.; Shcherbakov, M. R.; Miroshnichenko, A. E.; Neshev, D. N.; Fedyanin, A. A.; Kivshar, Y. S. *Nano Letters* **2016**, 16, 4857-4861.

[15] Gili, V. F.; Carletti, L.; Locatelli, A.; Rocco, D.; Finazzi, M.; Ghirardini, L.; Favero, I.; Gomez, C.; Lemaître, A.; Celebrano, M.; De Angelis, C.; Leo, G. *Optics Express* **2016**, 24, 15965-15971.

[16] Camacho-Morales, R.; Rahmani,R.; Kruk, S.; Wang, L.; Xu, L.; Smirnova, D. A.; Solntsev, A. S.; Miroshnichenko, A.; Tan, H. H.; Karouta, F.; Naureen, S.; Vora, K.; Carletti, L.; De Angelis, C.; Jagadish, C.; Kivshar, Y. S.; Neshev, D. N. *Nano Letters* **2016**, 16, 7191–7197.

[17] Carletti, L.; Locatelli, A.; Stepanenko, O.; Leo, G.; De Angelis, C. *Opt. Express* **2015**, 23, 26544-26550.

[18] Aharonovich, I.; Englund, D.; Toth, M. *Nat. Photonics* **2016**, 10 (10), 631.

[19] Sergeyev, A.; Geiss, R.; Solntsev, A. S.; Sukhorukov, A. A.; Schrempel, F.; Pertsch, T.; Grange, R. *ACS Photonics* **2015**, 2, 687-691.

[20] Curto, A. G.; Volpe, G.; Taminiau, T.H.; Kreuzer, M. P.; Quidant, R.; van Hulst, N. F. *Science* **2010**, 329, 930-933.

[21] Lee, K. G.; Chen, X. W.; Eghlidi, H.; Kukura, P.; Lettow, R.; Renn, A.; Sandoghdar, V. *Nat. Photonics* **2011**, 5, 166-169.

[22] Checcucci, S.; Lombardi, P.; Rizvi, S.; Sgrignuoli, F.; Gruhler, N.; Dieleman, F. B. C.; Cataliotti, F. S.; Pernice, W. H. P.; Agio, M.; Toninelli C. *Light: Sci. & Appl.* **2017**, 6, e16245.

[23] Carletti, L.; Locatelli A.; Neshev, D. N.; De Angelis, C. *ACS Photonics* **2016**, 3, 1500–1507.

[24] Carletti, L.; Rocco, D.; Locatelli, A.; De Angelis, C.; Gili, V. F.; Ravaro, M.; Favero, I.; Leo, G.; Finazzi, M.; Ghirardini, L.; Celebrano, M.; Marino. G.; Zayats, A. V. *Nanotechnology* **2017**, 28, 114005-114015.

[25] Iwaszczuk, K.; Bisgaard, C.; Andronico, A.; Leo, G.; Jepsen, P.-U. *IEEE Trans. THz Sci. Technol*. **2013,** 3, 192.

[26] Fong, B. H.; Colburn, J. S.; Ottusch, J. J.; Visher, J. L.; Sievenpiper, D. F. *IEEE Trans. Antennas and Propagation* **2010** 58, 3212-3221.

[27] Gehrsitz, S.; Reinhart, F. K.; Gourgon, C.; Herres, N.; Vonlanthen, A.; Sigg, H. *J. Appl. Phys.* **2000**, 87, 7825-7837.

[28] Ohashi, M.; Kondo, T.; Ito, R.; Fukatsu, S.; Shiraki, Y.; Kumata, K.; Kano S. S. *J. Appl. Phys.* **1993**, 74, 596-601.

[29] Kruk, S. S.; Camacho-Morales, R.; Xu, L.; Rahmani, M.; Smirnova, D. A.; Wang, L.; Tan, H. H.; Jagadish, C.; Neshev, D. N.; Kivshar, Y. S. *Nano Letters* **2017**, 17, 3914–3918.

[30] Ghirardini, L.; Carletti, L.; Gili, V.; Pellegrini, G.; Duò, L.; Finazzi, M.; Rocco, D.; Locatelli, A.; De Angelis, C.; Favero, I.; Ravaro, M.; Leo, G.; Lemaître, A.; Celebrano, M. *Opt. Letters* **2017**, 42, 559–562.

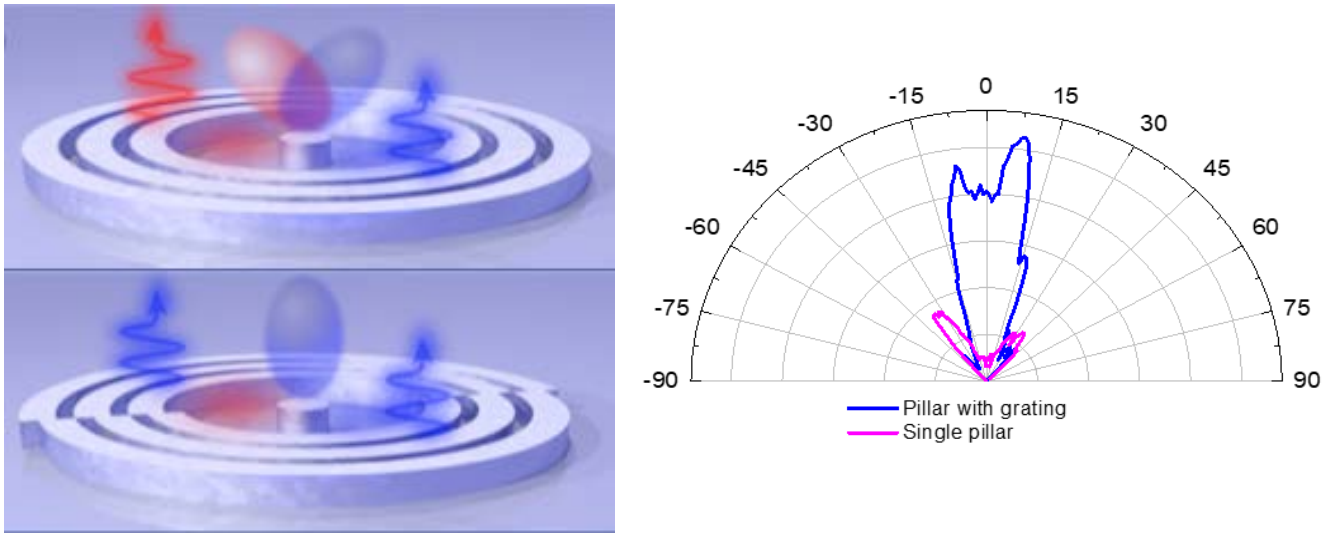
0
-15
15
-30
30
-45
45
-60
60
-75
75
-90
90
Pillar with grating
Single pillar

TOC Figure